Raman and photoluminescence spectra of $Zn_{1-x}Cd_xSe/Zn_{1-y}Mn_ySe$: A diluted-magnetic-semiconductor superlattice

R. G. Alonso, Eunsoon Oh, and A. K. Ramdas
Department of Physics, Purdue University, West Lafayette, Indiana 47907-1301

H. Luo, N. Samarth, and J. K. Furdyna
Department of Physics, University of Notre Dame, Notre Dame, Indiana 46556

L. R. Ram-Mohan
Department of Physics, Worcester Polytechnic Institute, Worcester, Massachusetts 01609
(Received 11 April 1991)

The luminescence spectrum of $Zn_{1-x}Cd_xSe/Zn_{1-y}Mn_ySe$ superlattices grown by molecular-beam epitaxy on (001) GaAs substrates shows quantum-well confinement and Zeeman shifts due to wave-function penetration into the barrier that are in excellent agreement with calculations using the transfer-matrix method based on the $\mathbf{k}\cdot\mathbf{p}$ formalism. The new periodicity introduced by the superlattice causes zone folding of the acoustic branch, allowing modes with large q vectors to become Raman active. The Raman spectrum shows the folded acoustic phonons of superlattices with as few as ten periods. In addition to the excitonic Zeeman shifts, these magnetic superlattices exhibit the Raman-electron paramagnetic resonance of Mn^{2+} typical of the Mn-based diluted magnetic semiconductors.

I. INTRODUCTION

As is well known, nonequilibrium growth techniques such as molecular-beam epitaxy (MBE) and metal organic chemical vapor deposition have enabled the fabrication of semiconductor heterostructures (epilayers, quantum wells, and superlattices) with constituents having submicrometer dimensions. Novel physics as well as optoelectronic applications have motivated the development of this area, mostly based on the ternary alloys of III-V semiconductors. In recent years much interest has been generated in extending the field to include II-VI semiconductors. Their impressive span of energy gaps (zero for the Hg-based compounds to 3.8 eV for ZnS), successful growth of lattice-matched as well as strained-lattice II-VI/II-VI and II-VI/III-V combinations in the context of quantum-well structures, surprising band offset situations, magnetic interactions associated with the incorporation of transition metal ions in a II-VI compound (e.g., $Cd_{1-x}Mn_xTe$) all are illustrative of the exciting features that can be realized in MBE-grown II-VI heterostructures.

The incorporation of a transition-metal ion like Mn^{2+} in a II-VI semiconductor such as CdTe results in a diluted magnetic semiconductor (DMS).[1] We note that the magnetic ions in materials of this type replace the group-II element in a random fashion. A DMS exhibits striking magnetic effects, most of which can be observed spectroscopically. For example, giant Faraday rotation[2] and large spin-flip Raman shifts of donor bound electrons[3] in the Mn-based DMS's originate from the large *sp-d* exchange interaction between the conduction and/or valence-band states and the *d* electrons of Mn^{2+}. This *sp-d* exchange interaction also carries over into the DMS submicrometer quantum-well structures.

We have previously studied Raman, photoluminescence, and modulated reflectivity spectra of $ZnSe/Zn_{1-x}Mn_xSe$ and $Cd_{1-x}Mn_xTe/Cd_{1-y}Mn_yTe$ superlattices,[4] and MBE-grown $Cd_{1-x}Mn_xSe$ and $Cd_{1-x}Zn_xSe$ epilayers.[5] The barriers in the superlattices studied in the present paper consist of $Zn_{1-x}Mn_xSe$, which in the bulk exhibits the zinc-blende structure for $0\le x\le 0.30$ and the wurtzite structure for $0.30<x\le 0.57$.[1] The well constituent of the superlattices investigated is $Zn_{1-x}Cd_xSe$, which in the bulk is also expected to have the zinc-blende structure for low x and the wurtzite structure for high x. A recent study[5] has shown, however, that epilayers of $Zn_{1-x}Cd_xSe$ grown by MBE on GaAs substrates exhibit the zinc-blende structure throughout the entire composition range $0\le x\le 1$. Similarly, when incorporated in a superlattice, both $Zn_{1-x}Cd_xSe$ and $Zn_{1-y}Mn_ySe$ have the cubic zinc-blende structure. The lattice parameter of these alloys increases linearly with x and y, respectively; thus one can minimize the lattice mismatch at the interfaces by selecting an appropriate combination of x and y and fabricate a superlattice with minimum or no strain. In this paper, we report an investigation of the DMS superlattice family $Zn_{1-x}Cd_xSe/Zn_{1-y}Mn_ySe$ using photoluminescence and Raman scattering.

II. EXPERIMENTAL PROCEDURE

The $Zn_{1-x}Cd_xSe/Zn_{1-y}Mn_ySe$ superlattices used in the present study were grown by MBE on (001) GaAs substrates. The sample parameters are given in Table I. The sample quality and layer thickness were determined by x-ray diffraction. Information on the MBE growth

TABLE I. Parameters for samples investigated: d_w and d_b are nominal well and barrier widths, respectively, D is the period (d_w+d_b) as calculated from the position of the folded phonons, and n is the number of periods.

Sample	Well	Barrier	d_w (Å)	d_b (Å)	D (Å)	n	Orientation
1	$Zn_{0.80}Cd_{0.20}Se$	$Zn_{0.80}Mn_{0.20}Se$	100	100	214	50	[001]
2	$Zn_{0.88}Cd_{0.12}Se$	$Zn_{0.80}Mn_{0.20}Se$	100	100	188	50	[001]
3	$Zn_{0.88}Cd_{0.12}Se$	$Zn_{0.80}Mn_{0.20}Se$	45	70	116	50	[001]
4	$Zn_{0.88}Cd_{0.12}Se$	$Zn_{0.80}Mn_{0.20}Se$	135	100	237	50	[001]
5	$Zn_{0.87}Cd_{0.13}Se$	ZnSe	50	50	117	100	[001]
6	$Zn_{0.85}Cd_{0.15}Se$	ZnSe	50	50	112	50	[001]
7	$Zn_{0.85}Cd_{0.15}Se$	ZnSe	60	60		10	[001]
8	$Zn_{0.85}Cd_{0.15}Se$	ZnSe	40	40		10	[001]

technique relevant to the superlattices investigated in this paper is given elsewhere.[6,7] The growth direction, also referred to as the superlattice axis, is designated by $\hat{z}$.

Raman spectra were excited with monochromatic radiation (with wavelengths λ_L) from Kr^+ or Ar^+ lasers. For low-temperature measurements the power of the incident beam was typically ≤ 75 mW in order to avoid sample heating. Measurements in an external magnetic field were carried out using a variable temperature optical cryostat with a superconducting coil providing external magnetic fields up to 60 kG. Scattered light was spectrally analyzed with a computer controlled double (triple) SPEX monochromator and detected with standard photon-counting electronics. The photoluminescence measurements were carried out on the same spectrometer.

III. RESULTS AND DISCUSSION

A. Photoluminescence

The photoluminescence spectra of superlattices yield the energy of the lowest quantum-confined level and reveal the quality of the heterostructure as deduced from the intensity and width of the luminescence peak. The comparison of the energy and Zeeman shift of the photoluminescence peak with the theoretically predicted values allows superlattice parameters such as well widths and valence-band offsets to be determined. Photoluminescence is also used in this investigation to establish the resonant conditions for Raman scattering.

The photoluminescence spectra of four $Zn_{1-x}Cd_xSe/Zn_{1-y}Mn_ySe$ superlattices studied in the present investigation are shown in Fig. 1. The characteristics of these superlattices are listed in Table I. The spectra were obtained at the temperature $T=5$ K with the 3638-Å uv line of an Ar^+ laser. The luminescence peaks shown are attributed to the excitonic recombination associated with the lowest quantum-confined electronic states, their energy being labeled as E_x(QC) in this paper. Since the barrier composition is the same in all the four superlattices, the differences in the position of the luminescence peaks in Fig. 1 can be traced to the well composition on one hand and the well and barrier widths on the other. The peak at the lowest energy corresponds to sample 1, the superlattice with the highest Cd concentration in the well, corresponding to the lowest bulk energy gap of the well material E_g(well)=2.586 eV. Superlattices 2, 3, and 4 all have the same composition, so that the effect of the well width on the energy of the luminescence peak is clearly observed. The peaks at 2.666, 2.686, and 2.710 eV correspond to superlattices with well widths $L_w=135$ Å (4), 100 Å (2), and 45 Å (3), respectively: the narrower the well, the higher the energy of the confined levels, i.e., as expected, all the three peaks are blue shifted from E_g(well)=2.656 eV. The energy gap of the well material is calculated from the x dependence of the energy gap in zinc-blende $Zn_{1-x}Cd_xSe$.[5]

In Fig. 2 the photoluminescence due to excitonic recombination is compared with that due to the 2.2-eV emission from Mn^{2+} in the $Zn_{0.88}Cd_{0.12}Se/Ze_{0.80}Mn_{0.20}Se$ superlattices, i.e., in samples 3 and 4. The spectra were again obtained at 5 K with the 3638-Å uv line of an Ar^+ laser. Note that the excitonic luminescence and the luminescence from Mn^{2+} are both observed in the same spectrum. This is significant, since in the photoluminescence spectrum of bulk DMS's (e.g.,

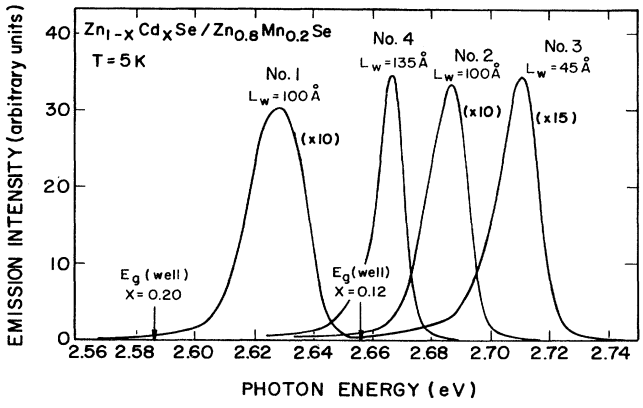

FIG. 1. Photoluminescence spectra of a series of $Zn_{1-x}Cd_xSe/Zn_{0.80}Mn_{0.20}Se$ superlattices (No. 1: $x=0.20$; No.'s 2, 3, and 4: $x=0.12$) showing the quantum-confined excitonic transition. The energy gap of the $Zn_{1-x}Cd_xSe$ well material is indicated with an arrow.

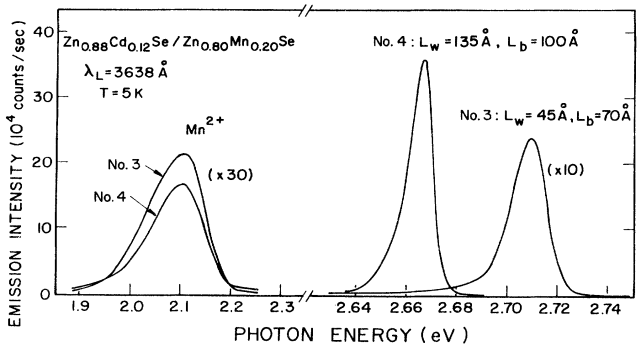

FIG. 2. Photoluminescence spectra of $Zn_{0.88}Cd_{0.12}Se/Zn_{0.80}Mn_{0.20}Se$ superlattices (No. 3: well width $L_w=45$ Å, barrier width $L_b=70$ Å; and No. 4: $L_w=100$ Å, $L_b=135$ Å) showing the luminescence from the quantum-confined excitonic transition and the Mn^{2+} emission.

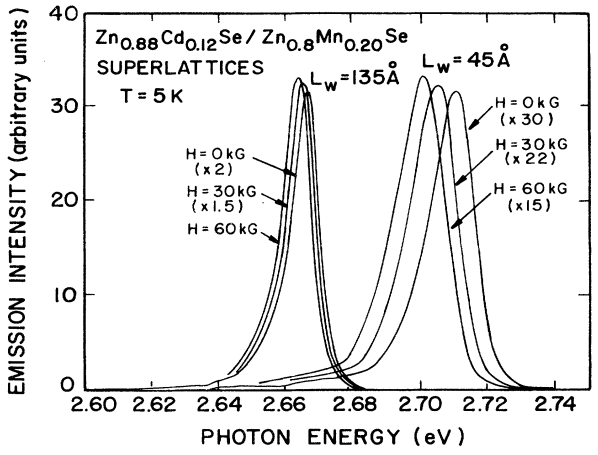

FIG. 3. Photoluminescence spectra for samples 3 and 4 showing Zeeman shifts at 5 K for $\mathbf{H}\perp\hat{z}$, the superlattice axis.

$Cd_{1-x}Mn_xSe$) only the Mn^{2+} luminescence is observed if the energy gap E_g is larger than the 2.2-eV emission line of Mn^{2+}.[8] The concurrent observation of Mn^{2+} and recombination luminescence is attributed to the spatial separation between the Mn^{2+} in the barriers and the electrons and holes in the well. Since the total well volume and the total barrier volume in sample 4 are larger than those in 3 (see Table I), both luminescence peaks are more intense in the former. We can define the quantum efficiency of the superlattice as the fraction of the number of incident light quanta that will generate an electron-hole pair whose recombination is detected in the photoluminescence spectrum. Assuming that the Mn^{2+} luminescence efficiency is independent of the well width, the ratio between the intensity of the exciton and that of the Mn^{2+} emission can be taken as a measure of the quantum efficiency of the superlattice. When the volume factors are taken into account, the peak intensities in Fig. 2 indicate that the quantum-well efficiency of sample 3 ($L_w=45$ Å, $L_b=70$ Å) is a factor of 2 or more larger than that of sample 4 ($L_w=135$ Å, $L_b=100$ Å). This suggests that narrower barriers allow wells to collect the incident radiation more efficiently, but a more extensive investigation is required to verify this hypothesis.

Figure 3 shows the photoluminescence spectra of samples 3 and 4 at magnetic fields **H** of 0 , 30, and 60 kG and $T=5$ K, **H** being perpendicular to the superlattice axis. In a magnetic field, the recombination radiation corresponds to the transition from the $|\frac{1}{2},-\frac{1}{2}>$ state of the conduction band to the $|\frac{3}{2},-\frac{3}{2}>$ state of the valence band. At 60 kG the Zeeman shift of the photoluminescence from bulk $Zn_{0.80}Mn_{0.20}Se$, the barrier constituent, is approximately 40 meV (see Ref. 9), while as seen in Fig. 3, the Zeeman shift of the quantum-confined transition in sample 3 is only 10 meV and that in sample 4 is even smaller, i.e., 2 meV. The larger Zeeman shift in sample 3, the superlattice with the narrower well, can be attributed to the larger penetration of the confined wave function into the magnetic barrier. Table II shows E_x(QC) and the associated Zeeman shift at $T=5$ K and $H=60$ kG characterized by the Brillouin function $B_{5/2}(g_{Mn}\mu_B H/k_B T)$, where μ_B is the Bohr magneton.

Previous studies[4,10] have shown a larger Zeeman shift

TABLE II. Energy of the quantum-confined excitonic transition E_x(QC) and of the Mn^{2+} emission (in eV) at 5 K. Also listed is the Zeeman shift for E_x(QC) at 60 kG. Calculated values of E_x(QC) and its Zeeman shift are given in the last two columns.

	E_x(QC) (eV)		Mn^{2+} (eV)	Zeeman shift at 60 kG (meV)	
Sample	Expt.	Theor.	Expt.	Expt.	Theor.
1	2.628	2.623		3	2
2	2.686	2.686		3	3
3	2.710	2.710	2.114	10	9
4	2.666	2.665	2.110	2	1

for $\mathbf{H}\|\hat{\mathbf{z}}$ as compared to $\mathbf{H}\perp\hat{\mathbf{z}}$ in $CdTe/Cd_{1-x}Mn_xTe$ superlattices grown along the [111] direction, a behavior not present in those grown along [001]. The dependence of the Zeeman shift on the orientation of $\mathbf{H}$ observed in the former was attributed to interface defects where excitons were preferentially localized. Motivated by these results, we have measured the Zeeman shifts for $\mathbf{H}\|\hat{\mathbf{z}}$ and $\mathbf{H}\perp\hat{\mathbf{z}}$ in samples 2 and 3, both grown along [001], and found that the magnitude of the Zeeman shift is the same for both $\mathbf{H}$ orientations, within experimental error. Thus the behavior of $Zn_{1-x}Cd_xSe/Zn_{1-y}Mn_ySe$ superlattices with $\hat{\mathbf{z}}\|$ [001] resembles that of $CdTe/Cd_{1-x}Mn_xTe$ superlattices with $\hat{\mathbf{z}}\|$ [001]. A Zeeman shift asymmetry with respect to the orientation of the magnetic field can also arise when the exciton radius is comparable or larger than the width of the magnetic layer. The absence of this asymmetry in the photoluminescence experiment thus appears to indicate that in the cases investigated here the well width exceeds the exciton radius.

In order to confirm the identification of the photoluminescence peaks with the quantum-confined levels and to verify whether the magnitude of the Zeeman shift is consistent with the picture of the wave function penetrating into the magnetic barriers, we have carried out a series of energy-band calculations. The theoretical model chosen considers the valence-band offset as a parameter that can be adjusted to fit the experiment results. Given the fact that some of our superlattices are not lattice matched, the theoretical model has to account for the effect of strain which contributes to the heavy-hole–light-hole splitting of the valence band of the strained well, in addition to the splitting already present due to the reduced symmetry of the superlattice.

The energies of the confined levels and the magnitude of the Zeeman shifts in these superlattices have been calculated using an eight-band Kane model Hamiltonian for each layer and the transfer-matrix method.[11] The set of basis functions used in the calculation is that of Weiler,[12] which follows a Pidgeon-Brown model consisting of eight combinations of s and p orbitals and spins appropriate for the symmetry of the Γ_6 conduction band, the Γ_8 valence band, and the Γ_7 split-off band. This yields an 8×8 Hamiltonian matrix for each layer. The wave functions in each layer must satisfy the boundary conditions of continuity at the interfaces. Following the formalism of the transfer-matrix method, the problem can be characterized by a 16×16 transfer matrix.

The Hamiltonian for a given layer is given by

$$H=-\frac{\hbar^2}{2m}\nabla^2+V(r)+\frac{1}{4m^2c^2}(\boldsymbol{\sigma}\times\nabla)\cdot\mathbf{p}+H_{\text{strain}}\ . \tag{1}$$

The presence of a magnetic field is included by introducing the minimal gauge substitution $\hbar k\rightarrow\hbar k+(e/c)A$.[10] The matrix elements of the strain-free Hamiltonian (with applied H field) are those given by Weiler.[12]

The deformation potential Hamiltonian is given by[13]

$$H_{\text{strain}}=C_c\sum_i\epsilon_{ii}-a_v\sum_i\epsilon_{ii}-b_v\sum_i\epsilon_{ii}(J_i^2-\tfrac{1}{3}J^2)-\frac{d_v}{\sqrt{3}}\sum_{i<j}\epsilon_{ij}\{J_iJ_j\}\ , \tag{2}$$

where C_c is the conduction-band deformation potential constant, a_v is the valence-band hydrostatic deformation potential constant, b_v and d_v are the shear deformation potential constants, and ϵ_{ij} are the components of the strain tensor. This latter term has been introduced to account for strain in the superlattice layer due to lattice mismatch. The strain in our set of samples varies from practically strain-free superlattices up to 1% strain. In the well, the strain along x is obtained from the lattice mismatch, while the strain along z is derived from the strain-stress tensor equations, and is given by $\epsilon_{zz}=-(2c_{12}/c_{11})\epsilon_{xx}$.

A computer program[11] has been used to solve for the energies and the corresponding wave functions in the superlattice in the presence of an applied magnetic field parallel to $\hat{\mathbf{z}}$. The input parameters used are the energy gaps E_g and Δ, the interband matrix element $\mathbf{p}$, the valence-band Luttinger parameters, the deformation potentials for each layer, and the dimensional parameters of the superlattice. The valence-band offset has been adjusted to match the experimental results for the lowest energy transition E_x(QC) and its Zeeman shift. This calculation was carried out for the magnetic superlattices listed in Table II. As seen in this table, the calculated values for E_x(QC) and the Zeeman shifts are in good agreement with the experimental results and are consistent with small valence-band offsets ($\sim$25 meV). A limitation of the present eight-band model is that it does not include the binding energy of the exciton. The above value for the valence-band offset is consistent with the previous result of Walecki *et al.*,[14] who studied the effect of magnetic field on the photoluminescence from a heterostructure of $Zn_{1-x}Cd_xSe/Zn_{1-y}Mn_ySe$ containing three quantum wells of 105-, 42-, and 20-Å well widths, respectively; they deduced the band offset from a variational analysis which included the excitonic effects.

B. Folded acoustic phonons

As is well known, one-phonon inelastic light scattering, i.e., Raman and Brillouin scattering, is produced by phonons of $\mathbf{q}$ vectors which satisfy $|\mathbf{q}|=2|\mathbf{k}_L|\sin(\phi/2)$, where $|\mathbf{k}_L|=|2\pi/\lambda_L|$ and ϕ is the angle through which the radiation is scattered. Thus the q's probed in the process range from 0 to a maximum of $2|\mathbf{k}_L|$. Since the allowed values of q for a crystal are confined to the first Brillouin zone, the maximum $|\mathbf{q}|$ is π/a, and hence in the first-order inelastic light scattering with visible excitation one encounters only the phonons with q's near the zone center (since $2|\mathbf{k}_L|\ll\pi/a$). For the acoustic branch, characterized by frequencies $\omega=v_sq$ in this range, (where

v_s is the sound velocity of the medium), the frequency shifts expected in Brillouin scattering are typically of the order of 1 cm^{-1} and cannot be detected with a grating monochromator due to stray (parasitic) light.

The situation is different in the case of a superlattice. Consider a superlattice consisting of alternating layers of thickness d_1 and d_2, respectively, and hence with a new period $d_1+d_2=D$. Also let the structure sustain a propagating acoustic wave along $\hat{z}$, which is characterized by the average elastic properties of the two types of layers. It is clear that for the acoustic branch the Brillouin-zone boundary will now be given by $\pm\pi/D$ and the conservation of q vector in the backscattering geometry is satisfied by $q=\pm q_{SL}+2\pi m/D$, where q_{SL} is the wave vector of the wave propagating through the superlattice, m being 1,2,3,. . . . In other words, these q's yield the "long-wavelength" excitations along $\hat{z}$ of the structure having a unit-cell dimension of D in that direction and for each m the Raman spectrum will display a doublet. The frequency shifts corresponding to $m=1,2,3,\ldots$, are significantly higher than those of the Brillouin components and can be discovered with a grating monochromator. The intensity of the mth order of these Raman lines, observed as a consequence of the zone folding of the acoustic branch, is deduced from a photoelastic mechanism[15] and is proportional to $(1/m^2)\sin^2(m\pi d_1/D)$.

For long-wavelength acoustic phonons, the superlattice can be considered as an elastic continuum. In this approximation, the dispersion relation for folded phonons propagating along the superlattice axis is given by[16]

$$\cos(q_z D)=\cos\left[\frac{\omega d_w}{v_w}\right]\cos\left[\frac{\omega d_b}{v_b}\right]-(1+\delta)\sin\left[\frac{\omega d_w}{v_w}\right]\sin\left[\frac{\omega d_b}{v_b}\right], \quad (3)$$

where d_w and d_b are the respective thicknesses of the well and the barrier layers, $D=d_w+d_b$, and $\delta=\frac{1}{2}(\rho_w v_w-\rho_b v_b)^2/(\rho_w v_w \rho_b v_b)$, where ρ and v are the densities and velocities, respectively.

The Raman-scattering spectrum of the folded longitudinal-acoustic phonons in $Zn_{1-x}Cd_xSe/Zn_{1-y}Mn_ySe$ superlattices 6 and 4 (see Table I for parameters) is shown in Fig. 4. The spectra were taken at 295 K in the backscattering configuration with $\lambda_L=4825$ and 4880 Å, respectively, i.e., in close resonance with the confined excitonic transition. Figure 5 shows the Raman spectrum of sample 3, where the second-order ($m=2$) peaks are also observed.

The dispersion relations obtained from Eq. (3) for samples 4, 3, and 2 are shown in Fig. 6. The values of the densities ρ were calculated from the lattice parameters[1] and atomic masses, while the velocities v along [001] are given by $v=\sqrt{c_{11}/\rho}$, where the elastic constants c_{11} were estimated by interpolation from the c_{11} values for the binary components of the mixed crystals given in Ref. 17. The Raman shifts are shown with dots, the size of the dots indicating the error bars. The wave-vector transfer in a backscattering experiment is given by

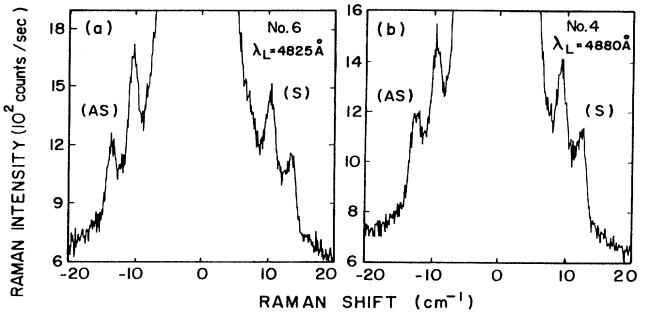

FIG. 4. Stokes (S) and anti-Stokes (AS) components of the folded longitudinal acoustic phonons in (a) $Zn_{0.85}Cd_{0.15}Se/ZnSe$ (No. 6) with laser power $P_L=80$ mW and (b) $Zn_{0.88}Cd_{0.12}Se/Zn_{0.80}Mn_{0.20}Se$ (No. 4) with $P_L=125$ mW. See Table I for parameters.

$q=4\pi n/\lambda_L$, where n is the refractive index of the sample. The lines in Fig. 6 have been calculated using a superlattice period D (D equals the well width plus the barrier width) which gives the best fit to the observed Raman shifts. The period deduced from the folded acoustic phonons is in agreement with the nominal values, as can be seen in Table I.

We note here that gaps in the phonon dispersion will appear at $q=0$ and $\pm\pi/D$ due to the periodicity D in the $\hat{z}$ direction of the superlattice.[16] Figure 6(d) shows an enlarged view of one of the small gaps in the dispersion relation for sample 3. It can be deduced from Eq. (3) that, for small δ, the size of the gap can be between zero and $2\sqrt{2\delta}/(d_w/v_w+d_b/v_b)$. Thus the size of the gap is related to the difference in density and elastic constants between the well and the barrier as measured by δ.

Although the position of the folded phonons is very

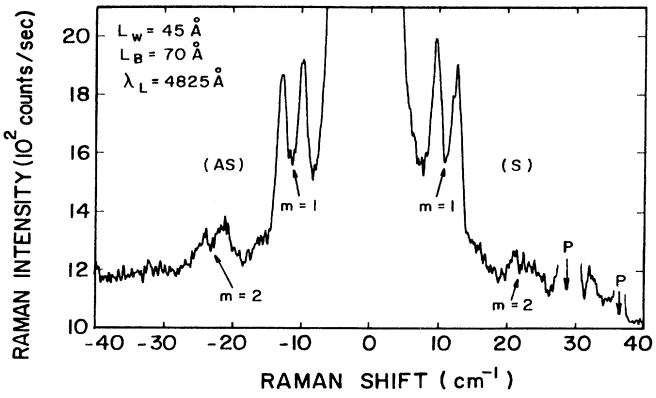

FIG. 5. Stokes (S) and anti-Stokes (AS) components of the folded longitudinal acoustic phonons in $Zn_{0.88}Cd_{0.12}Se/Zn_{0.80}Mn_{0.20}Se$ (No. 3). The lines labeled P are plasma lines from the Kr^+ laser.

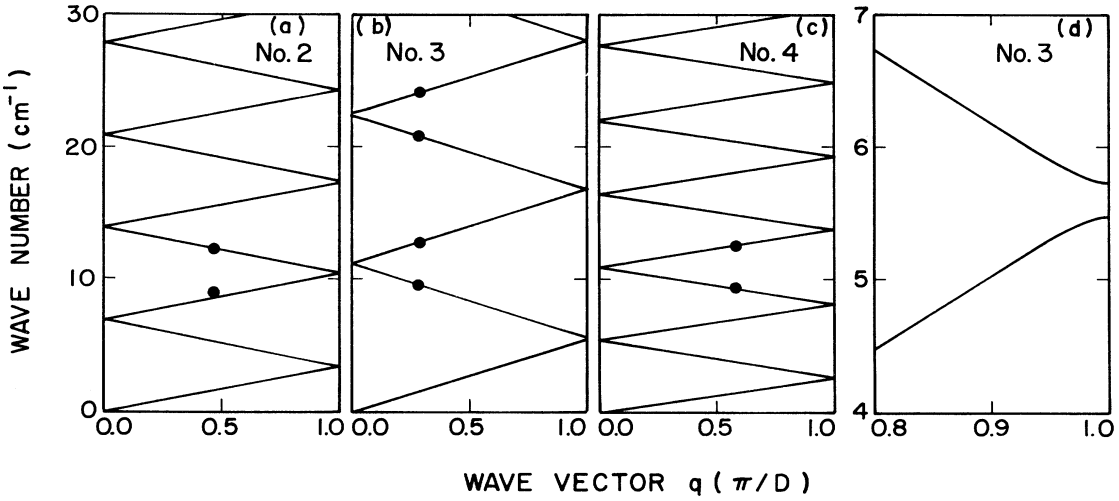

FIG. 6. Dispersion curves for the folded LA phonons calculated using the elastic continuum theory. Observed Raman shifts are shown with dots, the size of the dots indicating the error bars: (a) No. 2, (b) No. 3, and (c) No. 4. (d) Enlarged view of the first gap in the dispersion curve of No. 3.

sensitive to the period D of the superlattice, it is not difficult to show that the doublet splitting is relatively independent of D in the long-wavelength approximation.[15] In this limit, the superlattice sound velocity $v_{SL}=\omega/q$ is given by

$$v_{SL}=D\left[\frac{d_w^2}{v_w^2}+\frac{d_b^2}{v_b^2}+2(1+\delta)\frac{d_w d_b}{v_w v_b}\right]^{-1/2}, \quad (4)$$

and the doublet splitting is given by

$$\Delta\omega=2v_{SL}q=8\pi n v_{SL}/\lambda\ . \quad (5)$$

For sample 3, for example, we obtain $\Delta\omega=3.1$ cm^{-1}, in excellent agreement with the experimentally observed doublet splitting of 3.0 ± 0.1 cm^{-1} in Fig. 5.

Folded acoustic phonons have also been observed in $ZnSe/Zn_{1-x}Cd_xSe$ superlattices, including sample 8, a ten-period superlattice. In the latter case even though the continuum model is not very realistic, it is quite surprising that it can predict the phonon position to within a 20% accuracy considering that the phonon wavelength itself is about eight periods (almost the complete length of the superlattice). Finally, it should be remembered that the observation of folded acoustic phonons in the Raman spectrum is an indication of high interface quality,[18] thus demonstrating that the family of superlattices investigated here are structurally excellent.

C. Magnetic excitations

Magnetic excitations characteristic of bulk DMS's—such as the spin-flip transition within the Zeeman-split $3d^5$ multiplet of Mn^{2+}, i.e., the Raman electron-paramagnetic-resonance (EPR)—are expected to be observed in superlattices containing a DMS barrier or well. The intensity of this Raman line is resonantly enhanced when the energy of the scattered photon is close to that of a Zeeman component of the excitonic transition. This resonant enhancement demonstrates that the underlying mechanism for Raman-EPR involves interband electronic transitions.[19] The Raman EPR shift, given by $\hbar\omega_{PM}=g_{Mn}\mu_B H$, yields a g factor of 2, as expected for Mn^{2+}.

Figure 7 shows the Raman EPR lines in sample 2 at

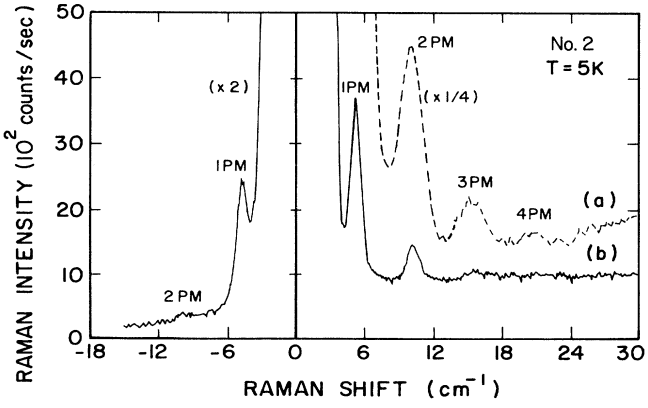

FIG. 7. Mn^{2+} Raman EPR lines in sample 2 at $T=5$ K. The Raman lines in (a) correspond to 1PM, 2PM, 3PM, and 4PM, which result from spin-flip transitions within the Zeeman multiplet of Mn^{2+}, i.e., from $mg\mu_B H$ with $m=1$, 2, 3, and 4, respectively. This spectrum is obtained in the crossed polarization $z(yx)\bar{z}$ with magnetic field $H=60$ kG along x and incident wavelength of 4579 Å. The spectrum in (b) shows the Stokes and anti-Stokes component of 1PM and 2PM lines observed with a smaller slit width.

$T=5$ K. This spectrum is obtained in the crossed polarization $z(yx)\bar{z}$, with incident wavelength of 4579 Å and magnetic field $H=60$ kG along x. The Raman-EPR lines labeled 1PM, 2PM, 3PM, and 4PM correspond to spin-flip transitions within the Zeeman multiplet of the Mn^{2+} ion, with energies $mg\mu_B H$, where $m=1$, 2, 3, and 4, respectively. In bulk crystals the presence of the multiple EPR lines 3PM and 4PM has been attributed to spin-flip transition within a coupled Mn^{2+} pair. In the case of the 100-Å magnetic layers in sample 2, the high intensity of the 3PM and 4PM lines can be attributed either to an increased number of Mn^{2+} pairs near the interface, or to the relaxation of the selection rules associated with the spherical symmetry, in which case the 3PM, 4PM, and 5PM lines become allowed in a single Mn^{2+} ion. Multiple EPR features of up to 7PM have been observed previously by Alonso *et al.*[5] in a $Cd_{0.9}Mn_{0.1}Se/ZnSe$ superlattice and were attributed to the presence of Mn^{2+} pairs, which can allow for such overtones.[5] The spectrum in Fig. 7 (b) shows the Stokes and anti-Stokes components of the 1PM and 2PM transitions observed with the spectrometer set to a smaller slit width.

IV. CONCLUDING REMARKS

Optical studies in heterostructures containing wide band-gap II-VI alloys offer the opportunity of observing transitions from quantum-confined levels with energies well into the blue region of the spectrum. The feasibility of laser action in the blue has generated considerable interest in these heterostructures. The presence of Mn^{2+} in II-VI heterostructures offers an additional probe into the quality and properties of the material. For example, in addition to the well and barrier widths and compositions, now the energies of the quantum-confined level transitions depend on the applied magnetic field in a pronounced manner, thus offering an additional sensitive characterization technique. In the present paper we have demonstrated that photoluminescence and Raman scattering can provide valuable information about the quality and properties of II-VI heterostructures containing DMS's. The study of the magnetic-field dependence of the photoluminescence in MBE-grown $Zn_{1-x}Cd_xSe/Zn_{1-y}Mn_ySe$ superlattices has provided insights into the nature of the wave functions of the quantum-confined levels, and in particular their penetration into the magnetic barriers. The interpretation of the effects leads to an understanding of the valence-band offsets. The lattice dynamics of the superlattices has provided characterization of their structural quality and their periodicity. It is very encouraging that high-quality complex structures from II-VI and II-VI-based DMS's can be fabricated with increasing success using MBE techniques.

ACKNOWLEDGMENTS

The work reported in this paper was carried out with support from the Defense Advanced Research Projects Agency-University Research Initiative Consortium on "Submicron Heterostructures and Optical Electronics in Wide-Gap II-VI Semiconductors and Related Compounds," administered by the Office of Naval Research (under Contract No. N00014-86-K-0760). The work at Purdue and at the University of Notre Dame also received support from the National Science Foundation, Grants No. DMR-89-21717 and No. DMR-89-13706, respectively.

[1]J. K. Furdyna, J. Appl. Phys. **64**, R29 (1988).

[2]J. A. Gaj, R. R. Galazka, and M. Nawrocki, Solid State Commun. **25**, 193 (1978); D. U. Bartholomew, J. K. Furdyna, and A. K. Ramdas, Phys. Rev. B **34**, 6943 (1986); Eunsoon Oh, D. U. Bartholomew, A. K. Ramdas, J. K. Furdyna, and U. Debska, *ibid.* **38**, 13 183 (1988); **42**, 5201 (1990).

[3]See the article by A. K. Ramdas and S. Rodriguez, in *Semiconductors and Semimetals,* edited by R. K. Willardson and A. C. Beer (Academic, New York, 1988), Vol. 25, p. 345.

[4]E.-K. Suh, D. U. Bartholomew, A. K. Ramdas, S. Rodriguez, S. Venugopalan, L. A. Kolodziejski, and R. L. Gunshor, Phys. Rev. B **36**, 4316 (1987).

[5]R. G. Alonso, E.-K. Suh, A. K. Ramdas, N. Samarth, H. Luo, and J. K. Furdyna, Phys. Rev. B **40**, 3720 (1989).

[6]N. Samarth, H. Luo, J. K. Furdyna, R. G. Alonso, Y. R. Lee, A. K. Ramdas, S. B. Qadri, and N. Otsuka, Appl. Phys. Lett. **56**, 1163 (1990).

[7]N. Samarth, H. Luo, J. K. Furdyna, S. B. Qadri, Y. R. Lee, R. G. Alonso, E.-K. Suh, A. K. Ramdas, and N. Otsuka, Surf. Sci. **228**, 226 (1990).

[8]R. G. Alonso, Y. R. Lee, Eunsoon Oh, A. K. Ramdas, H. Luo, N. Samarth, J. K. Furdyna, and H. Pascher, Phys. Rev. B **43**, 9610 (1991).

[9]This is an estimate based on the Zeeman shift of the recombination radiation in bulk $Cd_{0.9}Mn_{0.1}Se$ assuming comparable values for the *sp-d* exchange constants. The experimental results on $Cd_{0.9}Mn_{0.1}Se$ are those in E.-K. Suh, A. K. Arora, A. K. Ramdas, and S. Rodriguez (unpublished).

[10]X.-C. Zhang, S.-K. Chang, A. V. Nurmikko, L. A. Kolodziejski, R. L. Gunshor, and S. Datta, Phys. Rev. B **31**, 4056 (1985).

[11]L. R. Ram-Mohan, K. H. Yoo, and R. L. Aggarwal, Phys. Rev. B **38**, 6151 (1988).

[12]M. H. Weiler, in *Semiconductors and Semimetals,* edited by R. K. Willardson and A. C. Beer (Academic, New York, 1981), Vol. 16, p. 119.

[13]See Eq. (4.9) in A. K. Ramdas and S. Rodriguez, in *Progress in Electron Properties of Solids,* edited by R. Girlanda *et al.* (Kluwer Academic, Amsterdam, 1989), pp. 65–98; see also G. L. Bir and G. E. Pikus, *Symmetry and Strain-induced Effects in Semiconductors* (Wiley, New York, 1974).

[14]W. J. Walecki, A. V. Nurmikko, N. Samarth, H. Luo, J. K. Furdyna, and N. Otsuka, Appl. Phys. Lett. **57**, 466 (1990).

[15]C. Colvard, T. A. Gant, M. V. Klein, R. Merlin, R. Fischer, H. Morkoc, and A. C. Gossard, Phys. Rev. B **31**, 2080 (1985).

[16]S. M. Rytov, Akust. Zh. **2**, 71 (1956) [Sov. Phys.–Acoust. **2**, 68 (1956)]; see also S. Rodriguez, A. Camacho, and L.Quiroga, Superlatt. Microstruct. **3**, 371 (1987).

[17]*Semiconductors: Physics of II-VI and I-VII Compounds, Semimagnetic Semiconductors,* edited by K.-H. Hellwege, Landolt-Börnstein, New Series Vol. III/17b (Springer-Verlag, Berlin, 1982).

[18]D. J. Lockwood, J.-M. Baribeau, and P. Y. Timbrell, J. Appl. Phys. **65**, 3049 (1989).

[19]A. Petrou, D. L. Peterson, S. Venugopalan, R. R. Galazka, A. K. Ramdas, and S. Rodriguez, Phys. Rev. B **27**, 3471 (1983).